Geochimica et Cosmochimica Acta, Vol. 69, No. 13, pp. 3349–3365, 2005

0016-7037/05 $30.00 + .00

doi:10.1016/j.gca.2005.01.024

U-Th zonation-dependent alpha-ejection in (U-Th)/He chronometry

JEREMY K. HOURIGAN,* PETER W. REINERS and MARK T. BRANDON
Department of Geology and Geophysics, Yale University, P.O. Box 208109, New Haven, CT 06520–8109

(*Received August* 2, 2004; *accepted in revised form January* 13, 2005)

Abstract—Both theoretical and empirical evidence shows that intracrystalline U-Th heterogeneity in zircon can lead to biases in (U-Th)/He ages if not accurately accounted for in α-ejection corrections. We present a model for age correction for U-Th zoned crystals. We apply this to spherical and prismatic grains with bipyramidal terminations. The spherical calculation is simplistic but allows rapid calculation of the approximate effects of a wide variety of U-Th zoning patterns. The bipyramidal calculation is computationally intensive but permits an more complete estimate of the combined effects of crystal morphology and source zoning as relevant to zircon. Our principle findings are: (1) the assumption of U-Th homogeneity can result in errors of up to ~30% (in rare cases, higher) for ejection-corrected ages for typical grain sizes and realistic zonation. (2) Tetragonal prisms with bipyramidal terminations, which are typical of most zircons, exhibit bulk retentivities that can differ by several percent from models considering crystals with pinacoidal terminations. When extreme cases, such as dipyramids, are considered, the bias can exceed 10% or more. (3) Morphologic effects can be accounted for to better than 1% precision by using new second-order polynomial parameters that describe retentivity as a function of surface-area-to-volume ratio calculated through more complete analysis of crystal dimensions including the height of pyramidal crystal sections. We illustrate application of our model using U-Th concentration profiles determined from single zircons by laser ablation ICP-MS from zoned Tardree Rhyolite zircons.

1. INTRODUCTION

Since the modern resurgence of (U-Th)/He dating (Zeitler et al., 1987; Farley et al., 1996; Wolf et al., 1996), numerous studies have used (U-Th)/He thermochronometry to study a wide range of geomorphic and tectonic processes (House et al., 1998; Reiners et al., 2000; Stockli et al., 2000; House et al., 2001; Stockli et al., 2002; Armstrong et al., 2003; Ehlers et al., 2003; Reiners et al., 2003). More recent studies have exploited the relatively rapid ingrowth of He to date young volcanic deposits (Farley et al., 2002; Aciego et al., 2003; Davidson et al., 2004; Min et al., 2005), and to understand diffusive loss of He associated with wildfires (Mitchell and Reiners, 2003) and shock metamorphism of meteroites (Min et al., 2004). We address here an important source of error with (U-Th)/He dating–alpha ejection from crystals with a non-homogeneous U-Th distribution. Furthermore, we investigate age inaccuracy associated with the simplified geometries used in current bulk retentivity models (Farley, 2002).

Helium in minerals is primarily generated by radioactive decay of U and Th, and their intermediate daughter products, to Pb, and, to a lesser extent, by decay of Sm to Nd,

$$^4He* = 8^{238}U\left(e^{\lambda_{238}t}-1\right)+7^{235}U\left(e^{\lambda_{235}t}-1\right)+6^{232}Th\left(e^{\lambda_{232}t}-1\right)+{}^{147}Sm\left(e^{\lambda_{147}t}-1\right). \quad (1)$$

Each transformation in the decay chain results in the generation of an energetic alpha particle or helium nucleus. The alpha particles have sufficient kinetic energy that stopping distances are long (~15–20 μm) compared to the size of a typically analyzed grains (Farley et al., 1996). Consequently, an α-ejection correction factor (F_T) is required to account for those He atoms ejected from the crystal (Farley et al., 1996; Farley, 2002).

Farley et al. (1996) defined F_T as the fraction of radiogenic ^{4}He retained in the host grain. The He age is corrected for ejection loss of He by $t=t'/F_T$, where t' is the raw uncorrected He age, and t is the corrected age.

Monte Carlo modeling of alpha ejection from idealized crystal geometries (tetragonal prism with pinacoidal terminations for zircon and a finite cylinder for apatite) has been used to define an empiric second-order polynomial that represents F_T solely as a function of β, the surface-area-to-volume ratio of the grain (Farley et al., 1996; Farley, 2002). This analysis assumed uniform concentration of U and Th, although the effect of U-Th zonation on simplified spherical crystals was also considered. A number of studies have demonstrated that this estimated F_T provides corrected He ages that are accurate when compared with known emplacement ages for quickly-cooled zircon standards (e.g., Tagami et al., 2003), or produce compatible ages when compared with other low-temperature thermochronometers in intercalibration studies (Stockli et al., 2000; Kirby et al., 2002; Reiners et al., 2003; Reiners et al., 2004). Replicate (U-Th)/He ages have a two-sigma standard deviation of ~6%–10%, much greater than expected given typical formal analytical precision on He, U, Th, and Sm measurements, ~3%–4% (2σ). Common practice for assigning age uncertainty to unknowns is to multiply the calculated age by the relative standard deviation for replicate analyses of given mineral standard, thus precision for unknowns is limited by the reproducibility of standards.

The model presented here is motivated by the thought that grain shape and U-Th zonation may be important factors in causing overdispersion and bias in replicated He ages. Farley et al. (1996), Farley (2002), and Meesters and Dunai (2002) have considered the problem of U-Th zonation, but their work does

* Corresponding author: (jeremy.hourigan@yale.edu).

not provide a full analysis of the influence of zonation and grain shape on alpha ejection. This issue may be particularly important for zircon, which commonly shows easily recognizable zoning, as indicated by cathodoluminescence (CL), backscatter electron imaging, and ion microprobe U-Pb dating (see review by Corfu et al., 2003). While CL maps do not quantitatively image U content, there is an often observed qualitative negative correlation between U content and CL intensity, likely related to CL suppression due to reduced crystallinity in high-U, radiation damaged domains (Nasdala et al., 2003). U-Th inhomogeneity is recognized in apatite as well (Boyce and Hodges, 2001; Dempster et al., 2003; Boyce and Hodges, 2005), but is less well documented in the literature.

Some recent studies have shown that U-Th zonation does produce significant age bias in (U-Th)/He dating. For example, Tagami et al. (2003) reported zircon He ages for the rapidly cooled Tardee Rhyolite. The reported mean ejection-corrected age 78.8 ± 7.0 Ma is much older than the U/Pb zircon crystallization age 58.4 ± 0.7 Ma (Gamble et al., 1999). In contrast, the uncorrected He age 56.2 ± 5.4 Ma agrees well with the emplacement age. Tagami et al. (2003) showed that Tardree Rhyolite zircons commonly have U-rich cores and U-poor rims (imaged by intracrystalline spontaneous fission-track distributions) which produce nearly complete ^{4}He retention. Thus, the standard F_T correction overestimates the ^{4}He ejected resulting in "too-old" ages. In another example, single-grain zircon He dating of slowly cooled plutons by Reiners et al. (2004) showed that zircons with tips and rims enriched by a factor of 30 in U produced ages that were "too-young" compared with ages from non-zoned zircons. The accuracy of ejection corrected He ages from non-zoned grains was inferred using time-temperature curve determined from ^{40}Ar/^{39}Ar multi-diffusion-domain analysis of K-feldspar. Reiners et al. (2004) showed that by using an α-ejection correction that accounted for the zoning, the He ages for the zoned and unzoned zircons could be brought into agreement.

In this paper, we use a numerical model to evaluate the relationships between helium retentivity and U-Th distributions for styles of zonation typical for zircon. We consider spherical grains and also bipyramidal prisms; however, the model calculation can be easily extended to other grain shapes, and thus could be used to estimate α-ejection corrections for other commonly dated minerals, such as apatite and titanite. In some cases (e.g., commonly with titanite), a breakage correction may need to be added to deal with the fact that these phases are commonly fragmented (Farley et al., 1996; Reiners and Farley, 1999; Stockli and Farley, 2004). Our model deals solely with α-ejection for quickly cooled zoned samples and does not treat the combined effects of α-ejection and helium diffusion (e.g., Meesters and Dunai, 2002).

Routine use of our model requires a minimally destructive methodology for analyzing U-Th distribution that can be easily applied to individual crystals before dating. Preliminary work indicates that 213 nm laser ablation ICP-MS depth profiling on unmodified whole grains does not significantly disturb the He systematics. We present here modeling results and corrected ages based U-Th zonation depth-profiles of Tardree Rhyolite zircons to illustrate the technique. A future paper will provide a more complete report on this methodology.

Table 1. Summary of abbreviations and symbols used in the text.

$\vec{A}$	Final alpha resting position vector
$\vec{P}$	Parent nuclide position vector
$\vec{S}$	Alpha-particle trajectory vector
F_T	Homogeneous bulk retentivity
F_{ZAC}	Zonation-dependent bulk retentivity
m	Subscript representing mth isotope
$f_m(\vec{P})$	Local retentivity, continuous form
$f_m(x_i, y_j, z_k)$	Local retentivity of m, discrete form
$a_m(x_i, y_j, z_k)$	Alpha-productivity
i, j, k	Matrix indices in x, y, and z
Δ	Isotropic computational grid spacing
C_m	Concentration of isotope m
α_m	Alphas produced in decay chain of m
λ_m	Decay constant for m
r_i	Discrete radial position
R	Spherical grain radius
τ	Growth-progress variable
γ	Age bias
$\hat{N}_n$	Unit normal vector for nth crystal face
d_n	Distance of nth crystal face to the origin
β	Surface-area-to-volume ratio
L	Crystal length
W_1, W_2	Crystal widths
h	Average pyramid height

1.1. General Method

Consider a U or Th atom at position $\vec{P}$ (Table 1). Radioactive decay produces an alpha particle that moves in direction $\vec{S}$. The alpha particle comes to rest at

$$\vec{A} = \vec{P} + \vec{S} \tag{2}$$

The direction of $\vec{S}$ is random but its magnitude S, is the constant alpha stopping distance as specified by the average kinetic energy for all decays (Farley et al., 1996) (Table 2). In the absence of diffusion, ignoring nm-scale displacement of intermediate daughter products, and given sufficient time, spontaneous decay would result in a set of alpha particles uniformly distributed at a distance S around $\vec{P}$. If $\vec{P}$ lies in close proximity to a grain boundary some of these positions may fall outside of the host grain (i.e., α-ejection). We define the local retentivity $f(\vec{P})$ as the fraction of alpha particles generated at $\vec{P}$ that remain in the host grain. $f(\vec{P})$ can be determined by analytical integration for some simple grain geometries (e.g., Farley et al., 1996; Meesters and Dunai, 2002) but more complex grain shapes require solutions by numerical integration or Monte Carlo modeling (Farley et al., 1996; Farley, 2002).

In our model the bulk ^{4}He retentivity for an entire grain is given by integration over a three-dimensional grid. The nodes of the grid are defined by $x_i = \Delta i$, $y_j = \Delta j$, and $z_k = \Delta k$, where x, y and z are continuous Cartesian coordinates, and x_i, y_j and z_k are discrete positions within an isotropic grid with node spacing defined by Δ. The retention F_{ZAC} for an entire grain is defined by the weighted average

$$F_{ZAC} = \frac{\sum f_m(x_i, y_j, z_k) a_m(x_i, y_j, z_k)}{\sum a_m(x_i, y_j, z_k)}. \tag{3}$$

The function $a_m(x_i, y_j, z_k)$, represents α-productivity for an isotope m at position x_i, y_j, z_k, given by,

$$a_m = \alpha_m \lambda_m C_m \tag{4}$$

where α_m is the number of ^{4}He produced by the m^{th} decay chain, λ_m is the decay constant and C_m is the isotopic concentration. The a_m term serves as a weighting factor for the function $f_m(x_i, y_j, z_k)$, the local retentivity for an isotope m at position x_i, y_j, z_k. The summation symbols indicate summation over the full range for the indices i, j, k, and m, where, for this exercise, m corresponds to ^{238}U, ^{235}U, ^{232}Th and ^{147}Sm The subscript ZAC, meaning "zonation-dependent alpha correction," is used to distinguish F_{ZAC} as an estimate that includes the effects of zoning, and more realistic 3-D grain morphologies. This measure is in contrast to the standard estimate F_T, which is based on a uniform composition and on a more simplified grain shape.

Equation (1) lists four α-producing reactions, but for chemical compositions typical of zircon the effects of alpha ejection can be estimated by considering the most abundant isotopes, ^{238}U and ^{232}Th. Although the ^{235}U decay rate is ~6 times faster than that for ^{238}U and the two decay series generate similar numbers of α-particles (Eqn. 1, natural concentration of ^{238}U is 137.88 times that of ^{235}U. ^{147}Sm produces only one alpha particle per atom, Sm/U concentration ratios in zircon typically range from 0.5 to 0.01 (e.g., Belousova et al., 2002; Hoskin and Ireland, 2000), ^{147}Sm is 15% of total Sm, and the ^{147}Sm decay rate is 100 times smaller than that of ^{238}U. Furthermore, kinetic energy of decay is relatively low (2.235 keV) (Ziegler, 1977) resulting α-stopping distances of ~ 6 μm within typical minerals. Where mineral chemistry requires, the method could be extended to include additional isotopes using the full range of isotopes in (1), but we have omitted them here for computational efficiency.

The 3-D spatial variability of a_m given by Eqn. 3 and 4 allows estimation of F_{ZAC} for petrogenetically complex zircons such as those with high Th/U (0.5–1.0) cores, mantled by very low Th/U (<0.1) rims. All synthetic profiles shown here are run with constant Th/U. Modeling is done with LabVIEW code that is available from the authors upon request.

1.2. Spherical Model

Farley et al. (1996) modeled F_T using an analytical solution for the fraction of alpha particles retained as a function of both crystal size and variable source distribution within spherical grains. The spherical approximation provides a reasonable estimate of the bulk alpha retentivity when using the dimensions of an "equivalent sphere" (i.e., a sphere with the same surface-area-to-volume ratio as the dated grain) (Farley et al., 1996; Meesters and Dunai, 2002). Our spherical modeling approach is similar to that of Farley et al. (1996) but we generalize the formulation to allow for integration of arbitrary distributions of ^{238}U and ^{232}Th. In the spherical model, radial symmetry allows simplification of (3) to give,

$$F_{ZAC} = \frac{\sum_{i=0}^{R/\Delta} r_i^2 f_m(r_i) a_m(r_i)}{\sum_{i=0}^{R/\Delta} r_i^2 a_m(r_i)}, \tag{5}$$

where the radial distance from the center of the sphere is $r_i = \Delta i$, Δ is the spacing between nodes, and R is the radius of the sphere. The spherical geometry allows us to determine the local alpha retention for ^{238}U and ^{232}Th using,

$$f_m(r_i) = 1 - \frac{(R - S_m + r_i)(R + S_m - r_i)}{4 r_i S_m} \tag{6}$$

where S_m (Table 2) is the average α-stopping distance for mth isotope (Farley et al., 1996). Eqn. 4 provides the rest of the calculation.

Table 2. Average alpha stopping distances (μm) for zircon (Farley et al., 1996).

	Zircon	Apatite	Titanite
^{238}U	16.97	19.68	18.12
^{235}U	19.64	22.83	21.01
^{232}Th	19.32	22.46	20.68

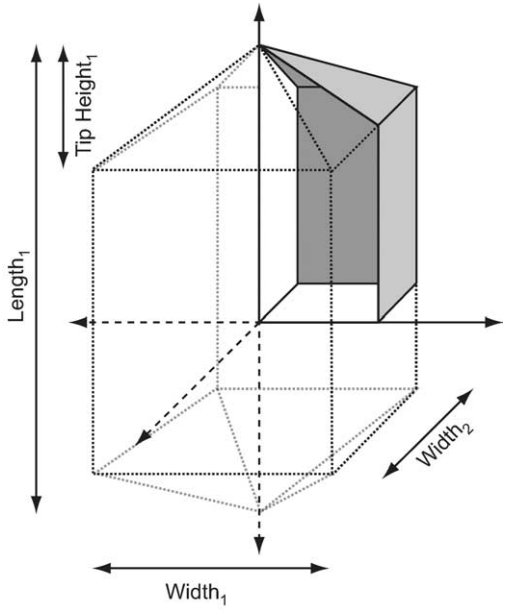

Figure 1. Geometrical construct for the idiomorphic crystal model, exploiting three-fold symmetry of the tetragonal crystal system to reduce computational overhead. Composition and local retentivity matrices are populated for points lying in the positive quadrant bounded by faces shown in grey. Equations for direction cosines of unit normal vectors and distances from individual faces to the origin are given in Table 3. Tip height is new measurement introduced here that allows for more explicit characterization of zircon morphology. Although the model considers only those decay sites lying within the positive quadrant simulation of local retentivity considers all crystal faces.

1.3. Idiomorphic Crystal Model

We extend our analysis to shapes and zoning relevant for zircon, which typically forms as pyramidally terminated tetragonal prisms (Fig. 1). To estimate F_{ZAC} for this case, 3-D matrices of $a_m(x_i, y_j, z_k)$ and $f_m(x_i, y_j, z_k)$ specified everywhere in the grain are constructed. The origin of the

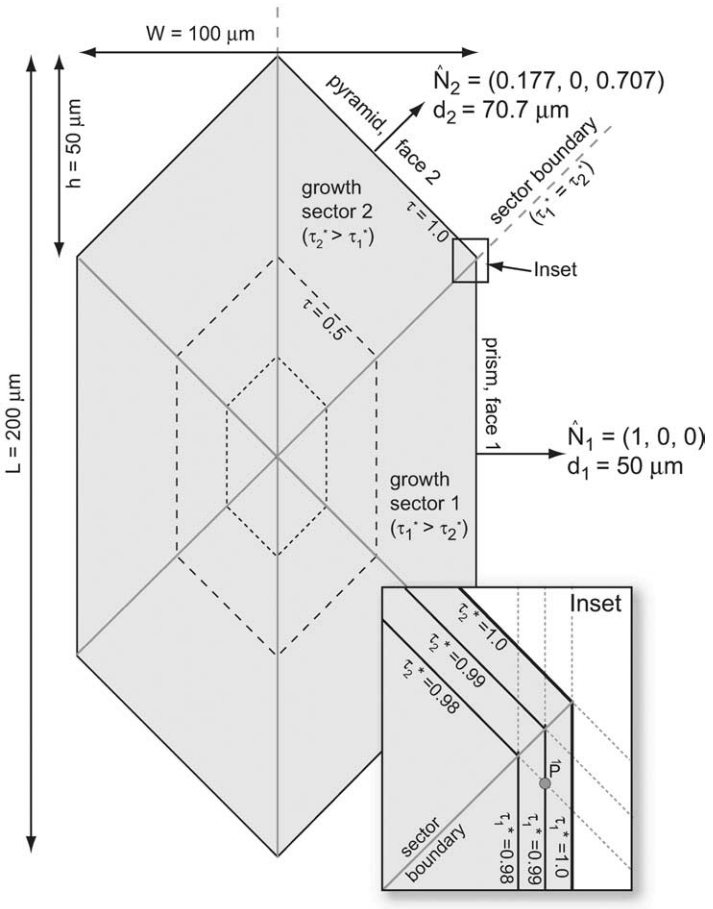

Figure 2. Construction of 3-D concentration matrix assuming self-similar crystal growth. The variable τ is the normalized (or fractional) distance to a given crystal face, n, in the direction parallel to the unit normal, $\hat{N}_n$. Growth sectors contain all points for which the variable τ is a maximum for the adjacent crystal face that controls outward, self-similar growth (e.g., growth sector A is produced by outward propagation of pyramid face 1). An isopleth of maximum τ values traces out small self-similar crystal form and represents an isochron or instant in the crystal's growth history. If the surrounding melt or fluid is partitioned into all sectors equally then a single 1-D zonation profile as a function of τ can be used to "grow" the full 3-D concentration distribution. **Inset**: isopleths of τ trial values, solid in the growth sector, dashed outside the corresponding growth sector. Examination of point $\vec{P}$ shows that the trial value τ_n^* is maximum for the face corresponding to the growth sector in which $\vec{P}$ resides. The parametric equations give $\tau_1^*(\vec{P} = 0.99$ and $\tau_2^*(\vec{P} = 0.98$, thus $\tau(\vec{P} = 0.99$.

coordinate system is placed at the center of the grain; tetragonal symmetry means that calculation need only consider those parent nuclides situated in the primary quadrant (x, y, $z \geq 0$) (Fig. 1). Ejection spheres centered in the primary quadrant may, however, protrude beyond faces in other quadrants thus the model considers full crystal when calculating local retentivity.

Grain dimensions are quantified using length and width measurements following standard (U-Th)/He lab protocol (Farley et al., 1996; Farley, 2002) with the addition of a new measurement, "tip height," which is the average of the measured heights, h, of the two pyramidal sections of crystal in question (Figs. 1, 2). The tip height parameter permits construction of an idiomorphic, bipyramidal tetragonal prism model crystal (Fig. 1). The grain geometry is defined by $\hat{N}_n$ an outward-directed normal vector of the nth crystal face (the hat indicates that the vector has unit length), and d_n, the minimum distance of that face from the origin (Table 3).

1.4. Local Retentivity.

The dot-product $\vec{P} \cdot \hat{N}_n$ represents the length of the projection of the position vector $\vec{P}$ of in the direction of the unit normal $\hat{N}_n$ for the n^{th} crystal face (Table 3). Points that lie outside of the grain are identified by the fact that they satisfy the inequality

$$\vec{P} \cdot \hat{N}_n > d_n \tag{7}$$

for at least one crystal face. The next step is to estimate f_m for points inside the grain. Where $(d_n - \vec{P} \cdot \hat{N}_n) \geq S_m$ for all faces, all $\vec{A}$ lie entirely within the grain and $f_m = 1$. Where one face has $(d_n - \vec{P} \cdot \hat{N}_n) < S_m$, the computation of f_m is provided by integration of a spherical cap extends beyond the face,

$$f_m = 1 - \frac{Area_{external\ cap}}{Area_{ejection\ sphere}} = 1 - \frac{S_m + \vec{P} \cdot \hat{N}_n - d_n}{2S_m}. \tag{8}$$

Table 3. Equations for unit normal vectors ($\hat{N}_n$) and distances to the origin (d_n) for crystal faces bounding a tetragonal prism with pyramidal terminations representative of typical zircon grains.

Section	n	Direction Cosines x	y	z	Distance d
Prism	1	0	-1	0	$\frac{W_2}{2}$
	2	1	0	0	$\frac{W_1}{2}$
	3	0	1	0	$\frac{W_2}{2}$
	4	-1	0	0	$\frac{W_1}{2}$
Top Pyramid	5	0	$\frac{-h}{\sqrt{h^2+W_2^2/4}}$	$\frac{W_2/2}{\sqrt{h^2+W_2^2/4}}$	$\frac{W_2 L}{4\sqrt{h^2+W_2^2/4}}$
	6	$\frac{h}{\sqrt{h^2+W_1^2/4}}$	0	$\frac{W_1/2}{\sqrt{h^2+W_1^2/4}}$	$\frac{W_1 L}{4\sqrt{h^2+W_1^2/4}}$
	7	0	$\frac{h}{\sqrt{h^2+W_2^2/4}}$	$\frac{W_2/2}{\sqrt{h^2+W_2^2/4}}$	$\frac{W_2 L}{4\sqrt{h^2+W_2^2/4}}$
	8	$\frac{-h}{\sqrt{h^2+W_1^2/4}}$	0	$\frac{W_1/2}{\sqrt{h^2+W_1^2/4}}$	$\frac{W_1 L}{4\sqrt{h^2+W_1^2/4}}$
Bottom Pyramid	9	0	$\frac{-h}{\sqrt{h^2+W_2^2/4}}$	$\frac{-W_2/2}{\sqrt{h^2+W_2^2/4}}$	$\frac{W_2 L}{4\sqrt{h^2+W_2^2/4}}$
	10	$\frac{h}{\sqrt{h^2+W_1^2/4}}$	0	$\frac{-W_1/2}{\sqrt{h^2+W_1^2/4}}$	$\frac{W_1 L}{4\sqrt{h^2+W_1^2/4}}$
	11	0	$\frac{h}{\sqrt{h^2+W_2^2/4}}$	$\frac{-W_2/2}{\sqrt{h^2+W_2^2/4}}$	$\frac{W_2 L}{4\sqrt{h^2+W_2^2/4}}$
	12	$\frac{-h}{\sqrt{h^2+W_1^2/4}}$	0	$\frac{-W_1/2}{\sqrt{h^2+W_1^2/4}}$	$\frac{W_1 L}{4\sqrt{h^2+W_1^2/4}}$

The integration of f_m is done numerically where two or more faces gives $(d_n - \vec{P} \cdot \hat{N}_n) < S_m$. A random-number generator is used to generate a uniform spherical distribution for $\vec{S}$. The final resting position for the ejected alpha particle is given by

$$\vec{A}_m = \vec{P} + \vec{S}_m = \begin{pmatrix} P_x + S_m\sqrt{1-u^2}\cos\theta \\ P_y + S_m\sqrt{1-u^2}\sin\theta \\ P_z + S_m\, u \end{pmatrix}, \qquad (9)$$

where $\theta \in [0,2\pi]$ and $u \in [-1,1]$ are variables selected randomly from the indicated ranges. Those particles that are ejected will give $\vec{A}_m \cdot \hat{N}_n > d_n$ for at least one of the crystal faces. $f_m(\vec{P})$ is given by the ratio of particles that remain within the grain relative to the total number of randomly generated particles. In our LabVIEW software, the number of Monte Carlo simulations is user-defined. Comparison with analytic solutions indicates that ~2500 points are needed to estimate f_m with errors <1%.

For crystals with uniform source distribution, the bulk retentivity F_{ZAC} is the sum of all array elements divided by the number of array elements inside the crystal.

Results of combined analytical and Monte Carlo simulation of local retentivity values are shown in 2-D slices through a 3-D matrix representing the positive quadrant of a 200 × 100 × 100 μm x 50 μm tip crystal with homogeneous parent distribution (Fig. 3a). This local retentivity map shows that the edges (two-face intersection lines), corners (three-face intersection points) and the apices (four-face intersection points) are regions of significantly reduced local retentivity. For instance, the apex of the pyramid with a "tip height" of 50 μm exhibits f_{238} values of ~0.16 (Fig. 3a). The effect of this reduced local

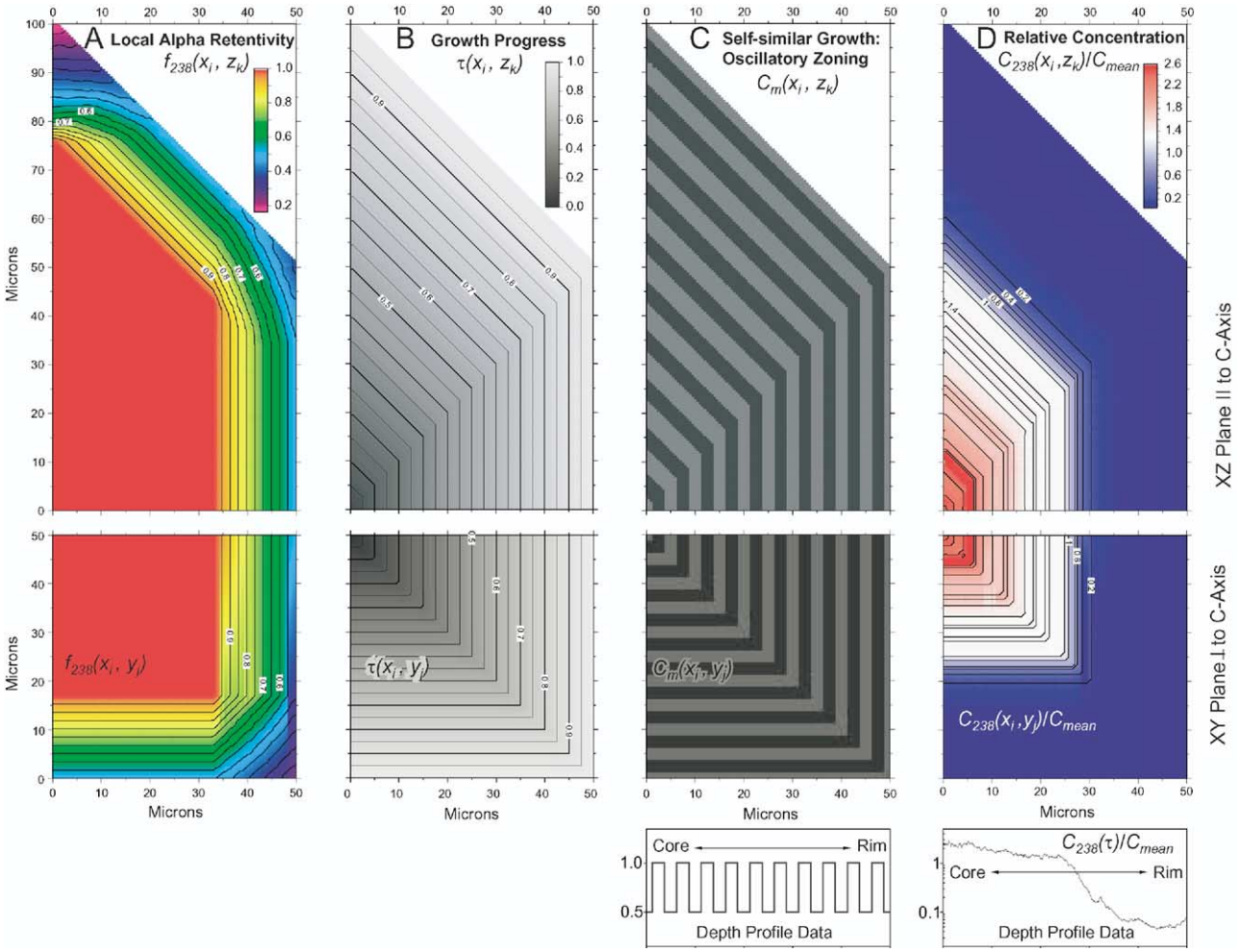

Figure 3. Contour plots for 2-D slices through 3-D matrices of local retentivity (3a), growth progress, τ (3b), a synthetic oscillatory zoning profile (3c) and normalized concentration based on a depth profile of a Tardree Rhyolite zircon (3d). Upper panels are section parallel to the A (x-axis) and C (z-axis) crystallographic axes at $y_j = 0$ μm. Lower panels are sections parallel to the A (x-axis) and B (y-axis) crystallographic axes and perpendicular the C-axis at $z_k = 0$ μm. F_{ZAC} parent nuclide in question is given by the sum of the product of the f_m (3a) and α-productivity (3c *or* 3d and (4)) divided by the summed α-productivity.

retentivity (relative to simplified geometries) can be amplified for cases such as U-Th-enriched tips resulting in dramatically lowered bulk retentivity because of the coincidence of minimal local retentivity and relative α-productivity values.

1.5. 3-D Representation of U-Th Concentration

The next phase in the modeling process is to map the full 3-D parent concentration distribution based one or more 1-D (depth profiles) or 2-D (e.g., fission-track density maps) measurements of concentration. To start, the model assumes that the external morphology of the zircon records the growth history of the crystal (e.g., Vavra, 1993) and that crystal growth progressed in a self-similar fashion starting at nucleation. This assumption constrains the relative growth rates of the crystal faces in directions parallel to their corresponding unit normal vectors. For example, for a 200 × 100 × 100 μm crystal with 50 μm tip height, the prism faces are 50 μm from the center of the crystal, whereas the pyramidal faces are d_n equal to 70.7 μm (Fig. 2). To account for the final geometry, the outward propagation of the pyramid face in the corresponding normal direction occurred 41.4% faster than the adjacent prism face in its unit normal direction.

As the crystal face grows outward, it leaves behind a growth sector (Fig. 2). The progress of growth within a growth sector is defined by

$$\tau = \frac{\vec{P}\cdot\hat{N}}{d}, \tag{10}$$

where $\hat{N}$ and d are for the parameters for the face related to that growth sector. For example, consider the two growth sectors in Figure 2. *Sector 1* contains all points through which *prism: face 1* propagated and the progress variable is given by,

$$\tau = \frac{\vec{P}\cdot\hat{N}_1}{d_1}. \tag{11}$$

Alternatively, *sector 2* (Fig. 2) contains all points through which *pyramid: face 2* propagated and the progress variable is given by,

$$\tau = \frac{\vec{P}\cdot\hat{N}_2}{d_2}. \tag{12}$$

The question is how to determine τ for an arbitrary point $\vec{P}$. We can use Eqn. 10 to calculate trial values for τ at $\vec{P}$ as a function of all possible faces in the crystal,

$$\tau_n^* = \frac{\vec{P}\cdot\hat{N}_n}{d_n}, \tag{13}$$

where n indicates the n^{th} face and the asterisk indicates a trial value for τ. The inset in Figure 2 shows that the solution for $\tau(\vec{P})$ is given by

$$\tau(\vec{P}) = \text{Max}\{\tau_1^*,\tau_2^*,\tau_3^*,\cdots\}. \tag{14}$$

Because we assume that growth is self-similar, surfaces connecting points of equivalent τ represent isochronal surfaces (Figs. 2, 3b) corresponding to an instant in the crystal growth history. Thus, (14) converts the position array in the space domain into the crystal-growth-time domain. If we assume that the partition coefficients of U and Th are uniform for all growth sectors (i.e., no sector zoning), then production of a full 3-D concentration distribution collapses to a simple function of τ.

Concentration depth profiles, $C_m(x)$, and (4) are used to construct the 3-D α-productivity matrix $a_m(x_i,y_j,z_k)$. If the profile is collected at the center of the prism section parallel to the unit normal for a given prism face (e.g., *prism: face 1* (Fig. 2)) the depth profile can be converted into a growth-time profile $C_m(\tau)$ by normalizing to the corresponding crystal face distance, d_1. Figure 3d shows the variation of normalized parent nuclide concentration in 2-D slices through a model crystal using actual U measurements from a LA-ICP-MS depth profile of a zircon from the Tardree Rhyolite. Figures 3a, c, and d show the distributions $f_{238}(x_i,y_j,z_k)$ and $C_{238}(x_i,y_j,z_k)$ used to estimate F_{ZAC}.

The assumption of self-similar crystal growth may be violated for natural zircons. We employ this assumption here as a simplification to understand, in theory, the combined effects of morphology and zonation. Comparison of synthetic profiles with a second, measured depth profile can be used to test the validity of our assumption on a crystal-by-crystal basis. The 3-D U-Th concentration maps produced by this model can be used to generate synthetic depth profiles positions corresponding to other depth profiles to conduct this comparison.

1.6. Surface-Area-to-Volume Ratio, β

Common practice for α-ejection correction is to model the bulk retentivity of multiple grains with variable dimensions and calculate polynomial fit parameters that give F_T as function of surface area to volume ratio of an equivalent sphere or tetragonal prism (Farley et al., 1996; Farley, 2002). We include here a general equation for β for orthorhombic crystals with pyramidal terminations

$$\beta(L,W_1,W_2,h) = \frac{2\left[(W_1+W_2)(L-2h)+W_1\sqrt{h^2+\frac{W_2^2}{4}}+W_2\sqrt{h^2+\frac{W_1^2}{4}}\right]}{W_1\times W_2\left[(L-2h)+\frac{2h}{3}\right]}. \tag{15}$$

Zircons commonly have widths W_1 and W_2 that are significantly different, despite being nominally tetragonal (e.g., Tagami et al., 2003). All idiomorphic model results shown below are for truly tetragonal grain morphologies ($W_1 = W_2$), although the code allows for variable widths.

2. RESULTS

2.1. Spherical Geometry

Eqn. 4–6 above allow modeling of α-ejection correction factors for a variety of U-Th zoning styles including linear, step, and arbitrary functions in spherical model-grains. Comparison of these zonation-dependent model results (F_{ZAC}) with homogeneous "standard" models (F_T) permits assessment of the age errors resulting from a priori assumption of U-Th homogeneity. The bias is measured using

$$\gamma = \frac{F_{ZAC}}{F_T} - 1 = \frac{t_T}{t_{ZAC}} - 1, \tag{16}$$

where t_T and t_{ZAC} are He ages correcting using F_T and F_{ZAC}, respectively. The results below consider only uranogenic alpha particles ($a_{238} = 1$) in zoned, quickly-cooled samples.

For most zonation styles, crystals of 25–30 μm radius exhibit maximum γ (Figs. 4a,b,d). Below this threshold, the majority of the volume of the crystal lies within one alpha stopping distance of the margin and has local retentivity values that are significantly less than unity, so the reduced retentivity due to high surface-area-to-volume outweighs intracrystalline zonation effects. Above this threshold, γ is smaller because more of the grain volume is fully retentive ($f = 1$). Steep concentration gradients give larger γ values. For the linear functions shown here (Figs. 4a,b), the magnitude of concentration change remains fixed but crystal radius varies, such that the concentration gradient is inversely proportional to crystal radius. For smaller crystals with larger concentration gradients, γ is larger. Grains with 10-μm thick, 10x enriched rim show less dramatic changes in γ relative to crystal radius than other models (Fig. 4c). This observation is attributed to the fact that the volume of the fixed-width rim scales with the cube of the crystal radius. As a result, the enriched rims contain a large fraction of the total parent nuclides in the crystal. Thus, even within large radii crystals, thin enriched rims can produce large errors if homogeneity is assumed.

Numerical integration allows for input of arbitrary radial concentration functions for zoning-dependent bulk retentivity calculation (Fig. 5a,b). Figure 5b represents alpha retentivity as a function of crystal size for a uranium zonation profile (1-D array of concentration as a function of depth (Fig. 5a) derived from laser-ablation ICP-MS depth-profiling of a Tardree Rhyolite zircon crystal). In this profile, the

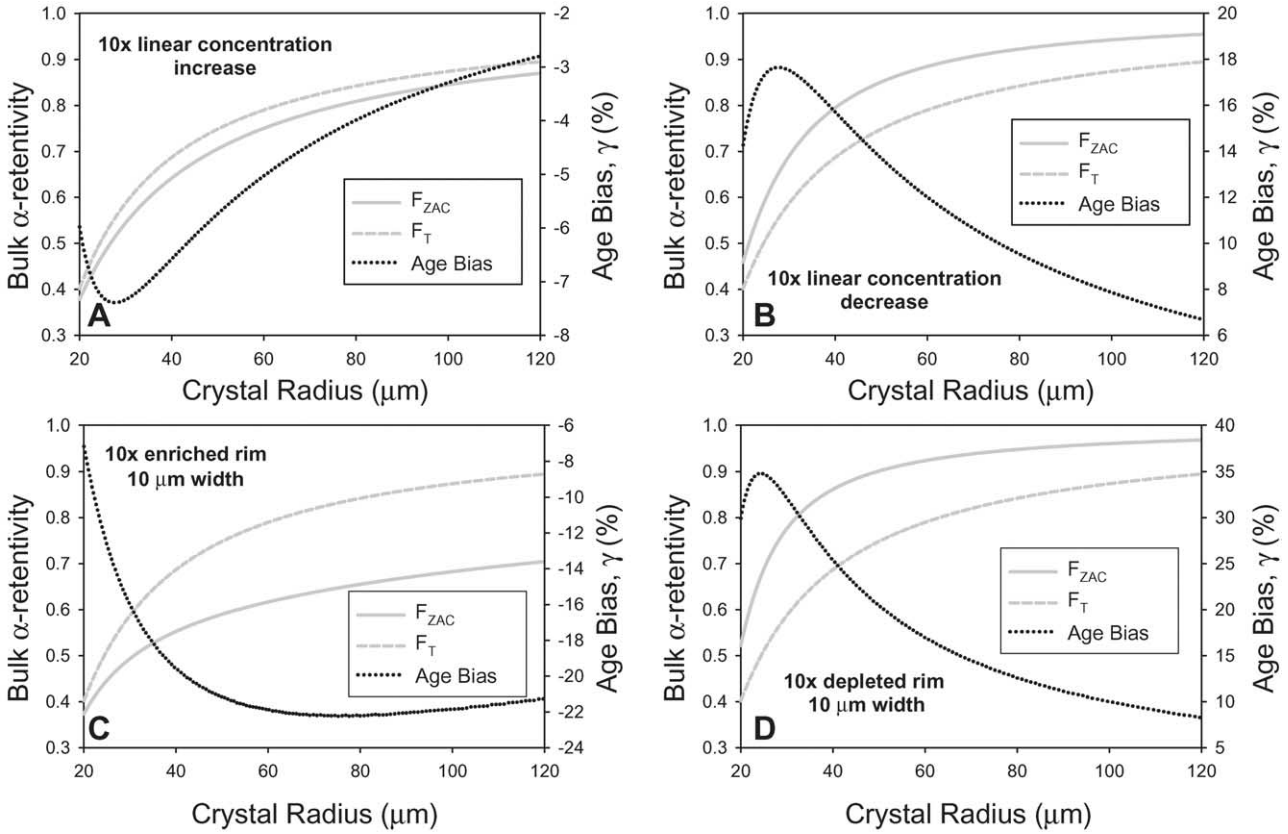

Figure 4. Alpha-ejection correction factor models for concentrically zoned spherical crystals. Homogeneous (F_T) and zonation-dependent bulk α-retentivity (F_{ZAC}) are plotted as a function of crystal radius. Age bias trends, γ, are shown as dotted lines (right-hand scale); see text and Eqn. 16. Zoning styles are: 1A) 10x linear concentration increase (core-to-rim), 1B) 10x linear concentration decrease, 1C) 10 μm 10x enriched rim, 1D) 10 μm 10x depleted rim.

rim is depleted in U by by as much as a factor of 40 (Fig. 5a) leading to age biases of ~+15 to ~+36% for crystals with equivalent-sphere radii of 80 μm and 40 μm, respectively, if a homogeneous U distribution were assumed. If imposed as the "mean" or characteristic zonation pattern for Tardree grains in the Tagami et al. (2003) study (F_T = 0.71) this profile would give an F_{ZAC} of 0.94 resulting in re-corrected age of 59.8 Ma, within 2.4% of the accepted U/Pb age and well within standard 2σ reproducibility of He ages on typical zircons (Reiners et al., 2004).

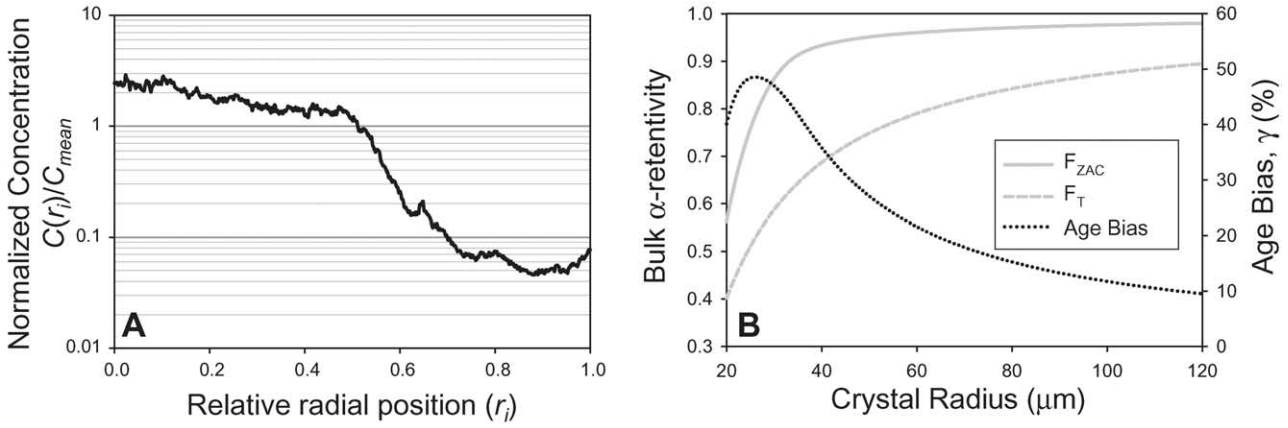

Figure 5. A. Measured laser ablation depth profile: normalized concentration as a function of relative radial position r_i from a Tardree Rhyolite zircon. This zircon shows extreme zonation, with core to rim U concentration contrast of ~40. **5B.** Spherical F_{ZAC} model results based on modeling of this depth profile. For typically analyzed crystal sizes of ~40–80 μm, predicted age bias values range from ~14% to ~36%.

The imaging techniques used to aid in situ ion microprobe zircon U/Pb geochronology have produced large body of literature describing, at least qualitatively, trace element zonation in zircons from a broad range of lithologies (see review by Corfu et al., 2003). Internal compositional structure of zircon can be highly variable, but rims featuring a sharp contrast in U-Th concentrations at a roughly concentric distance from the zircon interior are common features in some metamorphic and volcanic zircons, (e.g., Corfu et al., 2003). In such cases, U-Th zonation can be approximated as a step function of concentration (Meesters and Dunai, 2002; Reiners et al., 2004). Because such complex internal zonation is common in nature it is important to evaluate the degree of age bias expected for rims of varying width and concentration contrast magnitude (Fig. 6). Other variables held constant, decreasing crystal radius increases the degree of inaccuracy for ages of zoned, rimmed zircons where source homogeneity is assumed. Increases in the magnitude of concentration change across these step functions tend to increase the degree of age inaccuracy when other variables are fixed. Crystals with U-enriched rims show the most significant age biases across the widest range of conditions when compared with depleted rims (Fig. 6). Even relatively thin (<5 μm) rims enriched in U by a factor greater than four can produce large reductions in bulk retentivity ($\sim$-5%–12%). Furthermore, the reduction in bulk retentivity due to narrow rims does not diminish strongly with decreasing rim thickness (Figs. 6a-c). If enrichment magnitude is held constant and crystal size is allowed to vary, the rim thickness for which age inaccuracy maxima are observed remains relatively constant. Furthermore, the magnitude of maximum inaccuracy is nearly invariant across a wide range of crystal sizes. For example, a 4-μm thick 20x enriched rim, yields maximum age inaccuracy values of $\sim$-28% for 45 μm, 60 μm and 75 μm radii crystal models (Figs. 6a-c). This is due to the fact that the highly enriched rims carry a substantial fraction of the total U in the grain regardless of grain size, because of the cubic dependence of rim volume on radius.

The magnitude of age bias for depleted rims of fixed concentration change is more sensitive to crystal size than enriched rims. For example, inaccuracy maxima for 20x depleted rims are $\sim$+32% at 16.0 μm rim thickness for the 45 μm radius crystal model, +24% at 16.4 μm rim thickness for the 60 μm radius crystal model and + 18% at 16.6 μm rim thickness for the 70 μm. For all models inaccuracy maxima correspond to approximately one alpha stopping distance, or 16.97 μm (Figs. 6a-c) suggesting that depleted rim widths must approach one alpha stopping distance to significantly leverage the bulk retentivity. Unlike the enrichment case, narrow depleted rims do not significantly affect on the bulk retentivity.

2.2. Homogeneous Concentrations in Idiomorphic Crystals

Farley (1996) showed that surface-area-to-volume ratio (β) exerts first order control on bulk retentivity and established bulk retentivity vs. surface-area-to-volume relationships for cylindrical geometries approximating apatite crystals. Farley (2002) extended this to tetragonal prisms with pinacoidal terminations, more appropriate for zircon crystal morphologies. These polynomial fits for F_T as a function of β(L,W) method

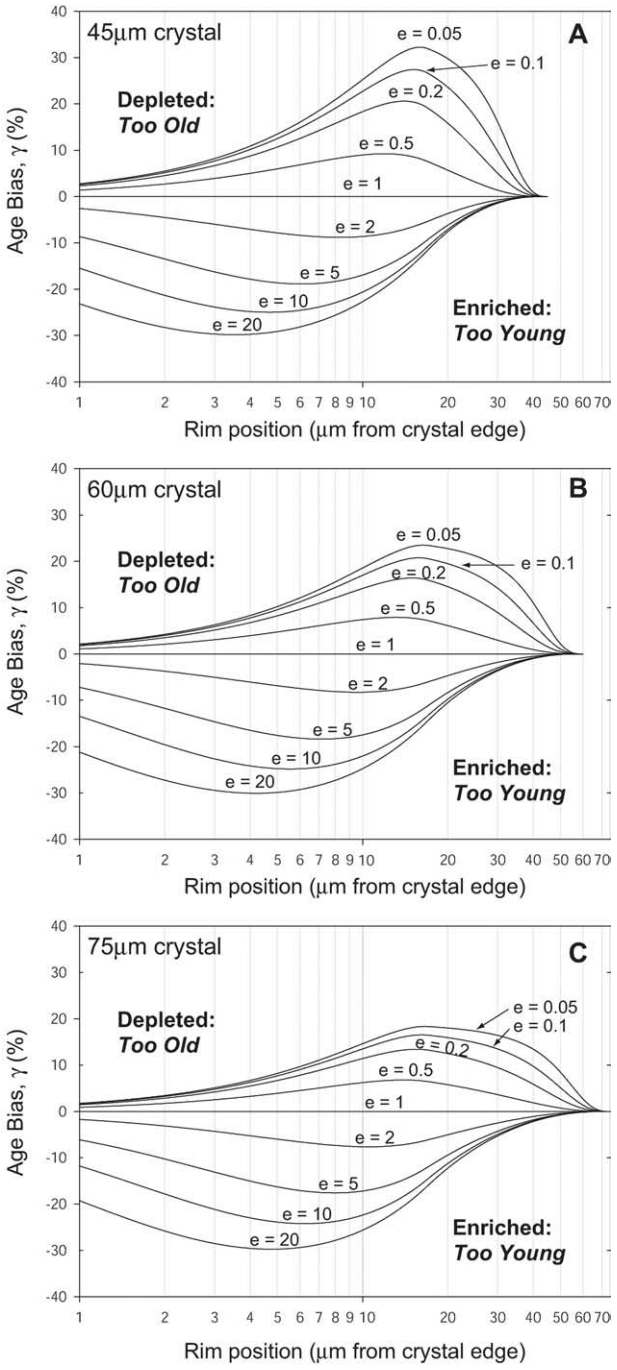

Figure 6. He age bias plots for spherical model crystals with rims (concentration step functions) of variable thickness and degree of enrichment or depletion. Modeled crystals have radii of 45 μm (2A), 60 μm (2B), 75 μm (2C). Rim widths are plotted on log scale to highlight the effects of fine (<10 μm) rims. Depleted rims lead to homogeneous α-corrected ages that are too old since bulk retentivity is underestimated. Conversely enriched rims produce corrected ages that are too young because bulk retentivity is overestimated. The inaccuracy associated with enrichment reaches a maximum $\sim$ 4–5 μm. Depleted rim inaccuracy is maximum on the order of one α-stopping distance (^{238}U). The magnitude of inaccuracy associated with depletion decreases significantly with crystal size whereas crystal size imparts little control on the magnitude of inaccuracy associated with rim enrichment.

Table 4. Comparison F_T vs. β polynomial fit parameters. Farley (Farley, 2002) parameters are derived from Monte Carlo modeling of pinacoidally terminated tetragonal prisms. Fit parameters are given for tetragonal prisms with both pinacoidal and pyramidal terminations. β-values are calculated for the pyramidal prism using equation 15. F_{ZAC} values for unknowns are given by, $F_{ZAC} = 1 + A_1\beta + A_2\beta^2$.

Parent Nuclide	Farley (2002)		This work (Tet.prism model)		This work (prism w/pyramids)	
	A_1	A_2	A_1	A_2	A_1	A_2
^{238}U	−4.31	4.92	−4.354	5.474	−4.281	4.372
^{232}Th	−5.00	6.80	−4.938	6.881	−4.869	5.605

provide a benchmark for the results of our 3-D idiomorphic crystal model run with uniform source distribution and pinacoidal terminations (i.e., tip height, $h = 0$ μm). Modeling variable length-to-width ratios for tetragonal prisms with pinacoidal terminations demonstrates that the effect of length-to-width ratio variation is small indicating that the surface-area-to-volume term captures most of the geometric effect on bulk retentivity (Farley et al., 1996). Polynomial fit parameters for the F_{ZAC} vs. β values for tetragonal prisms given by our numerical integration are in good agreement with those produced by the true Monte Carlo method (Farley, 2002) (Table 4). For the tetragonal prism models, our results agree to within $\pm$ 0.2% with Farley's over a β range of 0.03 to 0.1. We observe slightly greater misfit in the thorogenic helium retentivity relationship where our values are higher and vary between 0.2% ($\beta = 0.03$) and 1.2% ($\beta = 0.1$) (Table 4).

As conventional α-ejection correction protocol assumes pinacoidal terminations (Farley, 2002), it does not accurately treat the decreased retentivity within pyramidal sections (i.e., "tips") of real crystals. To understand this effect, we modeled tips of varying height from 0 μm (tetragonal prism with pinacoidal terminations) to one half-length (tetragonal dipyramid; no c-axis parallel faces). For these models we considered a range of common crystal lengths from 100 to 250 μm, and a typical length-to-width ratio of 2 (Fig. 7). The models were run with a computational mesh density of 4 nodes μm^{-1} to maximize the resolution of local retentivity in the crystal tips. Above 4 nodes μm^{-1}, arrays become too large for typical computational capabilities. For a 200 × 100 μm crystal with 25 μm pyramid heights a model with 4 nodes μm^{-1} yields a homogenous bulk retentivity of 0.7949; the same model with 3-, 2- and 1-nodes μm^{-1} yield values of 0.7944, 0.7934, and 0.7905, respectively. Thus, a four-fold reduction in computational mesh density is associated with a ~0.5% difference in modeled bulk retentivity while computer time is reduced by a factor of 64.

Figure 7 shows model F_{ZAC} as a function of β, using the method described above, for crystals with varying aspect ratios and pyramidal termination (tip) heights. The curves show a characteristic "hook shape" related to the decrease in surface-area-to-volume ratio for crystals with pyramidal heights that are small relative to their half-lengths (Fig. 7a). For example, a 100 × 50 μm crystal exhibits β minimum (0.0987) when its tip height is ~10 μm, whereas the tetragonal prism with pinacoidal terminations has a β of 0.1000

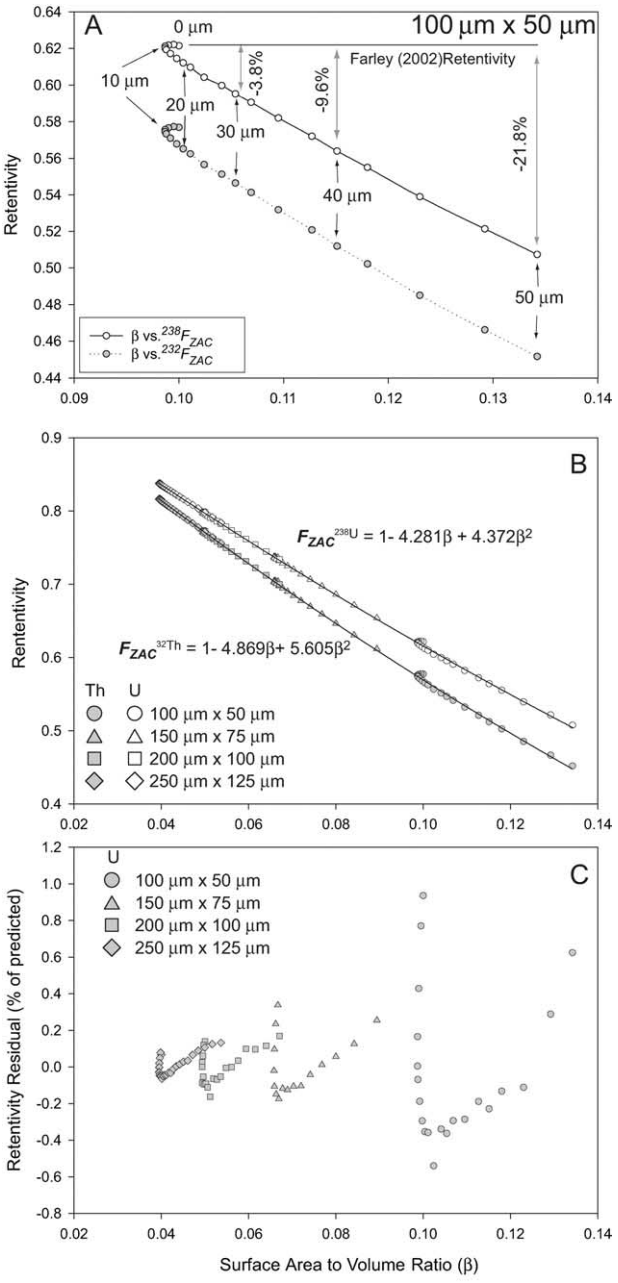

Figure 7. Bulk retentivity vs. surface-area-to-volume plots (6A, 6B) for tetragonal prisms with pyramidal terminations of variable height and length to width ratios of 2. 6A) 100 μm x 50 μm crystal shows characteristic hook shape related to the decreasing β ratio for tip heights from 0 to ~10 μm. Data are shown in 5 μm increments of tip height 6B) Retentivity data for 4 models crystals from 100 to 250 μm in length. The second-order polynomial fit differs slightly from that for tetragonal prisms with pinacoidal terminations. The characteristic hook shape is less evident here because the scale is expanded relative to 6A. The hook becomes less pronounced for larger crystals 6C) Bulk retentivity residuals vs. β. Here the residuals are the difference between calculated (using polynomial fit parameters and Eqn. 9 and modeled values for bulk retentivity. Increased misfit is observed for smaller crystal sizes, but indicate 0.1% to <1% uncertainty related to α-ejection correction for homogeneous crystals of typical size where tip height measurement is employed. Note that a 100 × 50 μm because the effect of tip height on bulk retentivity is most dramatic; typically analyzed zircons aliquots are 50%–100% larger than this model.

(Fig. 7a). The modeling shows that tetragonal prismatic crystals with stubby pyramids are more retentive than those with pinacoidal terminations because surface-area-to-volume ratio is slightly decreased. Increasing pyramid height beyond a threshold value, however, results in reduced retentivity due to increased alpha ejection from the apical section of the crystal (Fig. 7a). Generalization of this threshold in terms of a fractional tip height (i.e., tip height relative to half-length) is not straightforward. A 100 μm x 50 μm crystal attains maximum retentivity when the pyramidal section is ~2 μm, or 4% of the half-length, whereas a 250 μm x 125 μm crystal reaches a retentivity maximum at ~20 μm, or at 16% of the half-length.

F_{ZAC} vs. β model data for a range of crystal half-lengths and tip heights yield a slightly different set of polynomial fit parameters than those produced by tetragonal prisms alone (Fig. 7b) (Table 4). Our approach represents a significant departure from current α-ejection correction protocol in that we assign surface-area-to-volume ratios based on measurements of length, width prism faces and "tip height" assuming an idiomorphic tetragonal prism with pyramidal terminations (i.e., β(L,W,,h)) (Fig. 7a; Eqn. 15). This geometric oversimplification in previous models can result in propagation of significant error through the α-ejection correction, particularly for smaller crystals. As an extreme case, a 100 μm x 50 μm tetragonal dipyramid (i.e., h = 50 μm; the crystal is "all tip"), the modeled idiomorphic-crystal bulk uranogenic helium retentivity is 0.507 compared with the tetragonal prism retentivity at 0.618. Alpha-ejection correction using the latter value would result in an age that is 21.8% too young (Eqn. 16) (see Fig. 7a). It is important to note, however, that this model grain is much smaller than those that are typically analyzed, precisely because of the magnitude of the α-ejection correction (and its uncertainty).

The F_{ZAC} vs. β analysis enables assessment of the validity and uncertainty associated with calculation of α-ejection correction factors using second-order polynomial fits. Figure 7c shows the degree of misfit (in %) between individual F_{ZAC} models and the predicted values calculated using polynomial fit variables (Table 4). The fact that misfit exists indicates that the β term does not entirely capture all the geometric effects on bulk helium retentivity. However, in nearly all cases the residuals are significantly less than 1%, so the polynomial fit represents a decent approximation, particularly considering the present level of reproducibility typical for He dating. The degree of misfit increases as crystal size decreases; the residuals associated with a 250 × 125 μm crystal are ~0.1%, whereas the 100 × 50 μm crystal has residuals that range up to ~ 1.0% of the polynomial prediction (Fig. 7c). It is also worth noting that this modeling exercise provides assessment of crystal-size dependent uncertainties to the α-ejection correction factor applied in (U-Th)/He dating. If the conditions of U-Th homogeneity and idiomorphic crystal geometry are met for a single-crystal aliquot and there is no uncertainty associated with measurements of grain dimensions, the uncertainty on the α-ejection correction factor would be less than 1% for the typically analyzed range of grain sizes.

2.2.1. *Step-Function Zonation in Idiomorphic Crystals*

Like the spherical model, the idiomorphic crystal model can be used to investigate the effects of rims of varying thickness and concentration contrast on the bulk retentivity of tetragonal crystals with different prism termination morphologies. Figure 8a-c shows retentivity model results for 200 × 100 μm crystals with varying styles and extents of U-Th zonation, whose morphologies range from tetragonal prisms with pinacoidal terminations to dipyramids whose entire form is effectively pyramidal terminations. The correlation between bulk retentivity and rim thickness follows the same general principles as for the spherical case. Retentivity reduction relative to the homogeneous case is strongest for narrow, U-Th enriched rims, whereas the greatest relative retentivity increase occurs when rims are depleted in U-Th and are about one α-stopping distance in width. Figure 8d shows that model grains with pyramidal tips that comprise up to about half the total length of the grain result in retentivities within ~2%–3% of grains with pinacoidal terminations. However, zircons whose pyramidal terminations compose a majority of the grain length can produce retentivities significantly lower (by ~5%–8%) than those with purely pinacoidal terminations.

2.2.2. *Idiomorphic-Crystal Model – Spherical Model Comparison*

Meesters and Dunai (2002) asserted that the combined effects of alpha ejection and diffusion in crystals of arbitrary morphologies can be accurately modeled by translating the complex 3-D problem into a 1-D problem by modeling "equivalent spherical crystals." Here, we test the viability of the spherical approximation, for alpha ejection alone, by comparing results of our idiomorphic-crystal model with our spherical models of equivalent β (Fig. 9). The equivalent spherical radius is calculated from:

$$R_{eq} = \frac{3}{\beta(L, W_1, W_2, h)}. \quad (17)$$

Note that we use tip height (15) in the calculation of the equivalent radius. The equivalent radius value varies dramatically depending on crystal morphology, particularly for tip heights that are long relative to the crystal half-length. A 200 × 100 μm tetragonal prism with pinacoidal terminations has an equivalent sphere radius of 60 μm, 20% greater than the prism half-width. The same crystal with a 50 μm pyramidal terminations has an equivalent sphere radius of 58.6 μm, whereas the 200 × 100 μm dipyramid has a 44.7 μm equivalent sphere radius.

Another important question is whether rim width should be modified during tetragonal-to-spherical morphologic translation. The modeling below demonstrates that both crystal radius and rim thickness should be transformed into equivalent spherical lengths. Figure 9 shows the comparison of spherical and idiomorphic-crystal models for varying types of step-functions of U-Th zonation, with rims of varying concentration contrast, and thicknesses ranging from 1 to 50 μm (up to one half-width). Bulk retentivity values from our spherical model (*x*-axis) are plotted against modeled bulk retentivity for tetragonal

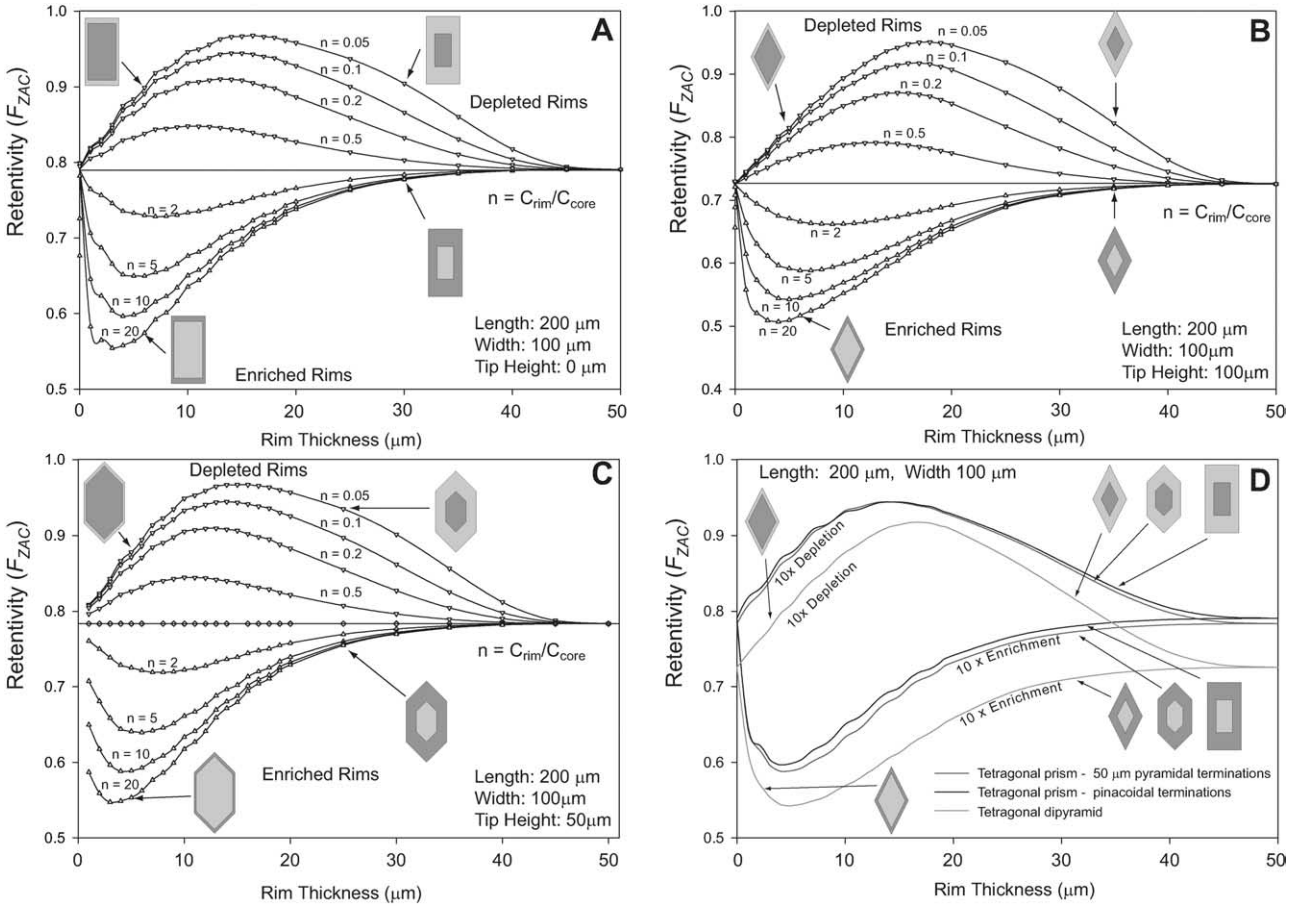

Figure 8. Zoning-dependent bulk retentivity plots for tetragonal model crystals with rims (concentration step functions) of variable width and degree of enrichment or depletion. The model crystal is tetragonal 200 × 100 μm with three different morphologies. 8A) tetragonal prism with pinacoidal terminations (tip height = 0 μm) 8B) tetragonal prism with pyramidal terminations (tip height = 50 μm), and 8C) tetragonal dipyramid (tip height = 100 μm). Figure 8D is a comparison of bulk retentivity for 10x enrichment and depletion step functions for the three morphologies. While the overall form of retentivity-vs.-rim-thickness curves are similar, the dipyramid morphology leads to significantly reduced retentivity.

prism with different types of termination morphologies (Fig. 9). The filled circles are model data for rim widths that are unmodified during transformation to the equivalent sphere, whereas open circles represent data for rim widths that have undergone a rim-width modification upon transformation of the grain to spherical geometry,

$$r_{sphere} = \frac{R_{eq}}{w_{1/2}} r_{real}, \tag{18}$$

where r_{sphere} is the transformed rim thickness, R_{eq} is the equivalent radius and $w_{1/2}$ and r_{real} are the half-width and rim thickness, respectively, of the idiomorphic crystal (Fig. 9). Contours show percent inaccuracy in bulk retentivity that would arise from application of spherical approximation to the real crystal morphology (Fig. 9). If unmodified rim widths (filled circles) are used, the inaccuracy associated with approximating realistic zircon morphologies as tetragonal prisms can be as high as ± 10%. However, transformation of idiomorphic crystal rim width by the same scaling factor as the sphere (Eqn. 18) improves the accuracy of the spherical approximation (Fig. 9 - open circles). In all cases this transformation reduces the inaccuracy of the spherical approximation to less than ± 2.5%, a level of uncertainty that may be acceptable for many thermochronometric applications. It should be noted that in this comparison, we did not scale alpha stopping distance proportionally to the spherical transformation, because it is not immediately clear how this should be done. Nevertheless, we expect that this would be a secondary effect, and suggest that these results show the utility of spherical approximation.

2.2.3. *Oscillatory zonation*

To illustrate the usage of the idiomorphic crystal model we present modeled bulk retentivity values for the three cases (Fig. 3b-d): homogeneous distribution, oscillatory zoning and a measured concentration depth profile through a zircon from the Tardree Rhyolite (Gamble et al., 1999; Tagami et al., 2003). Figure 3a shows the 2-D slices through a matrix of local retentivity. The average value for the local retentivity matrix, 0.786, represents the homogeneous bulk

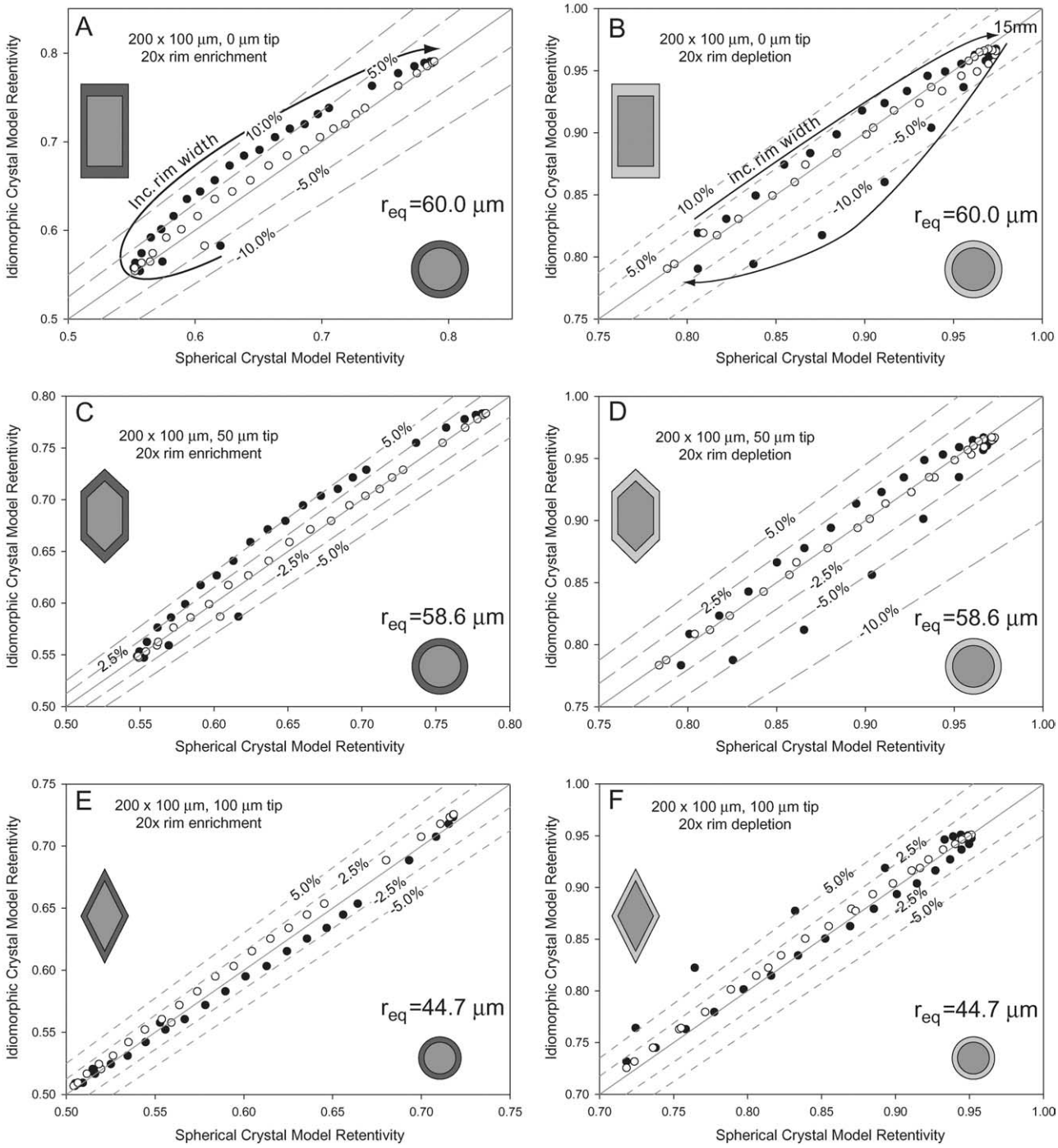

Figure 9. Six panels showing comparison between bulk retentivity results obtained using spherical and idiomorphic crystal models. Vertically distributed panels reflect different idiomorphic crystal morphologies: 9A,B) pinacoidally terminated tetragonal prism; 9C,D) 50 μm pyramidally terminated tetragonal prism; and 9E,F) tetragonal dipyramid. Horizontally distributed panels reflect rim style: 9A,C,E) enriched; 9B,D,F) depleted. Model starting conditions are a 200 $\times$ 100 μm idiomorphic crystal. X-axis data are the results of a spherical approximation following geometric transformation of the model idiomorphic crystal into an "equivalent sphere" of equal surface-area-to-volume ratios. Y-Axis data are idiomorphic crystal results shown in Figure 8. Filled circles are for models run with the same rim thickness in the spherical and idiomorphic crystal models. Open circles are run with modified rim widths reflecting the transformation to "equivalent radius" before spherical modeling (see text). Dashed lines are contours of bulk retentivity inaccuracy related to the spherical approximation. In panels 9A and 9B trends of increasing rim thickness are shown. The sign of misfit for the spherical approximation changes at rim widths corresponding to bulk retentivity maxima for depleted rims and minima for enriched rims. Transformation of rim width results in significantly reduced spherical approximation error.

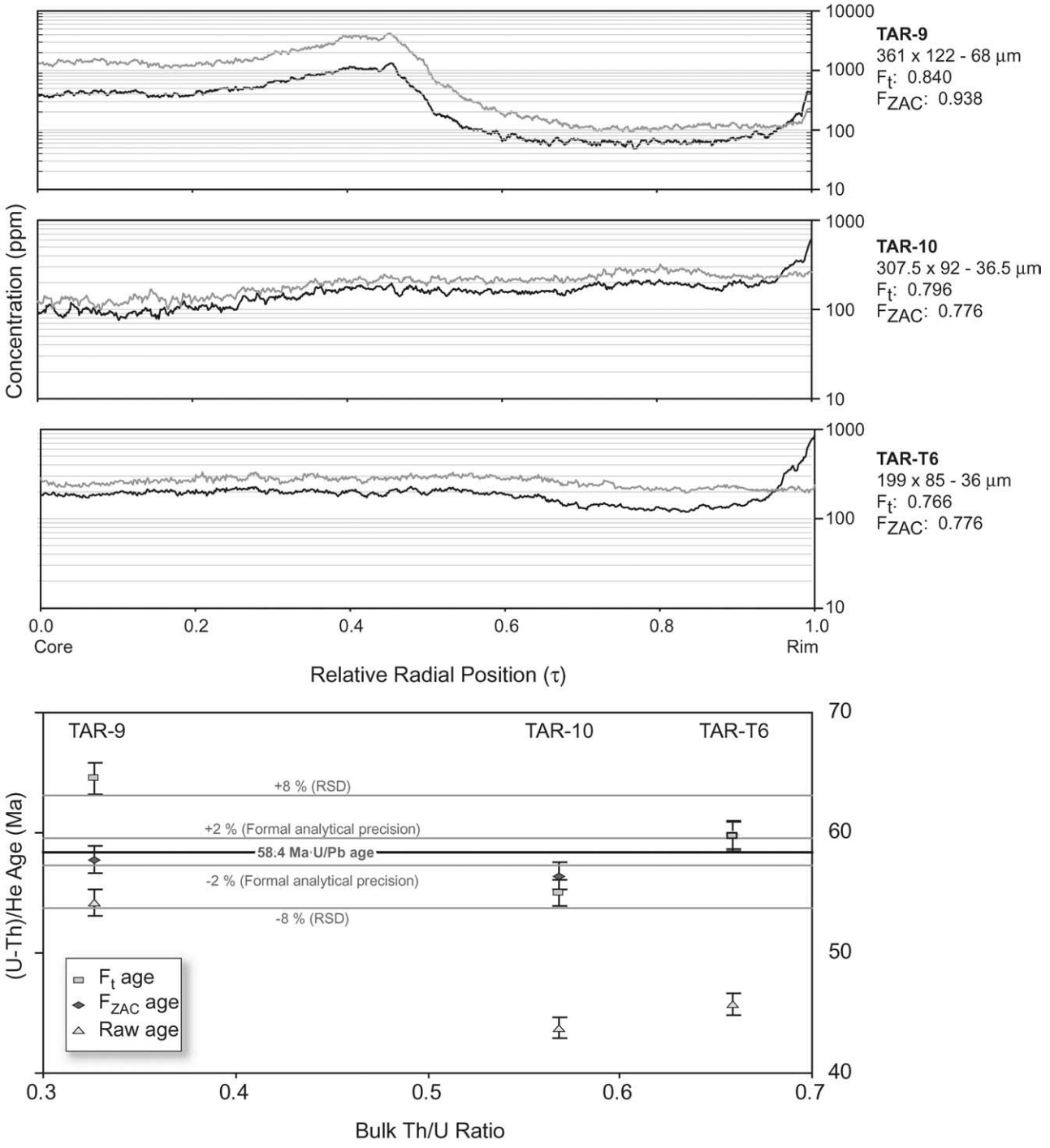

Figure 10. Three plots of U (grey) and Th (black) concentration depth profiles as a function of relative radial position (τ) for unmodified single grains of Tardree Rhyolite Zircon. Grain dimensions and model bulk retentivity values are given adjacent to each profile. (10A) TAR-9 shows dramatic broad zone of U-Th depletion (~0.025x) in the rim. (10B) TAR-10 shows moderate (2–3x) enrichment in the rim. (10C) U concentration varies by less than a factor of 1.5 over the entire TAR-T6 profile corresponding to virtual homogeneity for the purposes of α-ejection correction. (10D) Plot of raw ages, and homogenous and zonation-dependent α-ejection-corrected ages for the three depth profiles displayed above. Error bars for ages are show as 2% corresponding approximately to the 2σ formal analytical precision. All zonation-dependant corrected ages are of equivalent (TAR-T6) or higher level of grain-age accuracy than their homogenous counterpart. Note that F_{ZAC} and F_T ages are concordant so only the F_T age is shown on the plot

Table 5. Bulk retentivity modeling and (U-Th)/He age data for 3 grains of Tardree Rhyolite zircon with contrasting zonation patterns. Depth profiles and age data are shown in Figure 10. F_{ZAC}† indicates a spherical model was used.

Grain Measurements (μm)									Model Bulk Retentivity Values				
									Homogeneous			Zoned	
Sample	Length	Width	Width	Ave	Tip Height	β(L,W)	β(L,W,h)	a238	F_T	F_{ZAC}	F_{ZAC}†	F_{ZAC}†	F_{ZAC}
TAR9	361	121	123	122	68	0.0383	0.0384	0.892	0.839	0.840	0.834	0.943	0.938
TAR10	307.5	101	83	92	36.5	0.0500	0.0493	0.846	0.792	0.796	0.786	0.766	0.776
TAR-T6	199	81	89	85	35.6	0.0571	0.0569	0.830	0.764	0.766	0.755	0.766	0.764

						Alpha Ejection Corrected Ages (Ma)				
						Homogeneous			Zoned	
Sample	ncc 4He	ng U	ng Th	Th/U	Raw (Ma)	F_T	F_{ZAC}	F_{ZAC}†	F_{ZAC}†	F_{ZAC}
TAR9	2.58E+02	3.65E+01	1.19E+01	0.33	54.18	64.54	64.51	64.97	57.46	57.75
TAR10	1.11E+01	1.85E+00	1.05E+00	0.57	43.76	55.24	54.99	55.68	57.13	56.40
TAR-T6	6.19E+00	9.68E−01	6.38E−01	0.66	45.70	59.79	59.69	60.53	59.66	59.81

retentivity. Using our new polynomial fit parameters (Table 4) and β (L,W_1,W_2,h) we calculate a bulk retentivity of 0.788, within 0.4% of the modeled value. Figure 5c represents a synthetic oscillatory zoning profile expressed in 1-D below the two dimensional slices. The zonation-dependent bulk retentivity for this zoning profile in a 200 × 100 μm crystal is 0.786, only 0.01% less than the homogeneous model showing that fine-scale oscillatory zoning has essentially no effect on the bulk retentivity.

2.2.4. *Zonation-dependent α-ejection correction on a grain-by-grain basis*

Development of a methodology for collection of U-Th zoning profiles by laser ablation ICP-MS is ongoing. A future manuscript will deal specifically with the collection, concentration calibration and fractionation corrections necessary for deriving depth profile data, $C_m(x)$, from natural samples. Here we show modeling of the zonation-dependant bulk retentivity using U-Th depth profiles determined by LA-ICP-MS, with a few examples from natural zircons.

The mapping of the concentration distribution involves the assumptions that crystal growth proceeded self-similarly and that idealized depth profiling conditions (Mason and Mank, 2001) provide accurate 1-D U-Th concentration profile. Figure 3d shows 2-D slices through a 3-D concentration model constructed using the underlying depth profile. For this zoned case we calculate an F_{ZAC} value of 0.932, compared with F_{ZAC} 0.786 for the equivalent crystal with homogeneous U-Th distribution. The a priori assumption of homogeneity in this case would result in an 18.6% α-ejection overcorrection, and therefore a "too-old" (U-Th)/He age. For comparison, spherical modeling for this profile produces a bulk retentivity of 0.941, within ~1% of the idiomorphic result. Note however that the LabVIEW code automatically scales rim width for spherical models as discussed above.

Simplification of intracrystalline zonation patterns as simple step functions may represent an additional source of error in modeling of bulk retentivity. Here for instance the crystal might be modeled as having a step function at 20 μm depth with rim concentration depletion by a factor of 0.037 corresponding to the average concentration of the rim divided by the average concentration of the remaining 30 μm core. For the step-function, the spherical models yields an F_{ZAC} of 0.963 and the idiomorphic model gives an F_{ZAC} of 0.967 – a difference of less than 0.4%. The more dramatic disparity is observed between the step function, F_{ZAC} = 0.967, and the depth profile F_{ZAC} = 0.932, demonstrating that the simplification of real, potentially complex, zonation to step functions can be associated with large errors.

We analyzed several single-grain zircon aliquots from the Tardree Rhyolite, which is known to contain highly zoned zircon (Tagami et al., 2003) (Fig. 10; Table 5). We show three examples that exhibit different types of zonation given by LA-ICP-MS depth profiled Tardree Rhyolite zircons (1) depleted rim (TAR-9); (2) moderately enriched rim (TAR-10); and (3) near homogenous (TAR-T6) (Fig. 10). Modeled α-ejection correction factors are given adjacent to each depth profile. These depth profiles demonstrate that crystals within one sample can contain markedly different intracrystalline zonation patterns, highlighting the need for grain-by-grain characterization of zonation. The depth profile for TAR-9 yields the largest disparity between the homogeneous and zonation dependent α-ejection correction factors and ages (Fig. 10, Table 5). F_{ZAC} correction of the raw data yields an age of 57.8 ± 1.2 Ma (2%(2σ formal analytical precision)); F_T correction produces a "too-old" age of 64.5 Ma. TAR-10 exhibits only minor rim enrichment, requiring a lower α-ejection factor (0.776) compared with that for homogeneous U-Th distribution (0.796). F_{ZAC} age correction gives an age of 56.4 ± 1.2 Ma which is concordant with the accepted U/Pb age within 2σ analytical uncertainty. Finally the observed U-Th homogeneity in zircon TAR-T6 permits use of the homogeneous F_{ZAC} correction which produces an age of 59.8 ± 1.2 Ma. Here again the corrected age nearly reproduces the accepted age at the 2% analytical uncertainty level. In general, reproducibility on single-grain zircon (U-Th)/He ages, such as those from the Fish Canyon Tuff is ~6%–9% (2σ), significantly poorer than analytical uncertainty. The three examples shown here fall well within this 8% uncertainty envelope about the accepted age (Fig. 10), indicating that zonation dependent α-ejection correc-

tion by LA-ICP-MS may provide a reliable means for accurately dating zoned zircon populations.

3. CONCLUSIONS

We have derived a modeling approach that provides a more detailed understanding of the effects of U and Th zonation and realistic crystal morphology on helium retentivity for use in (U-Th)/He chronometry. Our emphasis was on zircon, although the principles could be applied to other minerals by modifying the geometric description used (e.g., Table 3) to reflect other crystal geometries and chemistries. The spherical and idiomorphic crystal morphology models shed new light on the magnitude of inaccuracy expected if the a priori assumption of compositional homogeneity is used to correct for alpha ejection from crystals with geologically realistic zoning styles. Spherical models are computationally simple and afford a general understanding of the effects of zoning on bulk He retentivity. This approximation yields retentivity values (α-ejection-correction factors) that are accurate to within ~2.5% provided that both the radius and its zonation pattern (or step-function rim width) are properly transformed based surface-area-to-volume and dimensions of the original grain.

Models for tetragonal prisms with pyramidal terminations demonstrate that bulk retentivity can be significantly reduced (e.g., up to 21% for a 100×50 μm tetragonal dipyramid) when compared to the tetragonal prism of the same length and width. These geometric effects can be accounted for to better than 1% accuracy using a modified second-order polynomial relating bulk retentivity to surface-area-to-volume ratio for idiomorphic crystals (i.e., $\beta(L,W_1,\ W_2,\ h)$). While computationally more intensive, the model simultaneously addresses the effects of source distribution, crystal size, and geometry on bulk retentivity for more realistic zircon morphologies and zoning style improved accuracy in (U-Th)/He dating.

The modeling approaches described in this paper extend the allowable range of morphologies and zonation patterns for aliquots routinely analyzed in (U-Th)/He thermochronologic studies. In cases such as bedrock investigations on plutonic rocks containing minimally zoned zircons, it may be possible to select crystal aliquots with dimensions that approximate pinacoidally terminated tetragonal prisms. However, one can envision other cases in which the level of zoning or crystal morphology do not afford the same level of aliquot selectivity. In addition, application of detrital thermochronology necessitates that the sampling strategy does not bias results by limiting the workable aliquots to a narrow range of morphologies or intracrystalline zonation. As (U-Th)/He thermochronologists seek to expand the temporal record of orogenic exhumation through detrital studies (e.g., Rahl et al., 2003), more sophisticated α-ejection correction models that treat effects of zonation, morphology and mechanical abrasion on helium retentivity will be required to avoid sampling bias resulting in omission or overrepresentation of elements of exhumational history.

Combined with LA-ICP-MS depth-profiling to characterize U-Th zonation on a our models can be used to estimate bulk helium retentivity on grain-by-grain basis before (U-Th)/He analysis. Ongoing and future work will be used to investigate whether: 1) unbiased single-grain, α-ejection-corrected (U-Th)/He ages can be routinely produced for zoned zircon samples such as Tardree Rhyolite; and 2) intracrystalline zonation is responsible for the overdispersion of the Fish Canyon Tuff zircon standard ages.

Acknowledgments—We thank Ed Bolton and Kyle Min for fruitful discussion, Andy Carter for providing the Tardree Rhyolite zircons, and Terry Plank, Katherine Kelly and Jennifer Wade at Boston University for assistance with LA-ICP-MS depth-profiling. Ken Farley and Dan Stockli provided thoughtful and thorough critical reviews which improved the final version of this manuscript. We acknowledge research support from National Science Foundation and to the Donors of The Petroleum Research Fund, administered by the American Chemical Society.

REFERENCES

Aciego S., Kennedy B. M., DePaolo D. J., Christensen J. N. and Hutcheon I. (2003) U-Th/He age of phenocrystic garnet from the 79 AD eruption of Mt. Vesuvius. *Earth and Planet Sci. Lett.* **216,** 209–219 doi:10.1016/S0012–821X(03)–00478-3.

Armstrong P. A., Ehlers T. A., Chapman D. S., Farley K. A. and Kamp P. J. J. (2003) Exhumation of the central Wasatch Mountains, Utah; 1, Patterns and timing of exhumation deduced from low-temperature thermochronology data. *J. of Geophysical Research* **108 (B3)**, 2172, doi:10.1029/2001JB0 **01708**, 2003.

Belousova E. A., Griffin W. L., O'Reilly S. Y., and Fisher N. I. (2002) Igneous zircon: trace element composition as an indicator of source rock type. *Contributions to Mineralogy and Petrology* **143,** 602–622.

Boyce J. W. and Hodges K. V. (2001) Chem. variations in the Cerro de Mercado (Durango, Mexico) fluorapatite: Assessing the effect of heterogeneity on a geochronologic standard, EOS Trans. AGU, 82(47), Fall Meet. Suppl., Abstract V22C-1061.

Boyce J. W. and Hodges K. V. (2005) U and Th zoning in Cerro de Mercado (Durango, Mexico) fluorapatite: Insights regarding the impact of recoil redistribution of radiogenic ^{4}He on (U-Th)/He thermochronology. *Chem. Geology* **219**(1-4), 261–274.

Corfu F., Hanchar J. M., Hoskin P. W. O. and Kinny P. (2003) Atlas of zircon textures. In *Zircon*, Vol. 53 (ed. J. M. Hanchar and P. W. O.. Hoskin), pp. 469–495. Mineralogical Society of America.

Davidson J. P., Hassanzadeh J., Berzins R., Stockli D. F., Bashukooh B., Turrin B. and Pandamouz A. (2004) The geology of Damavand Volcano, Alborz Mountains, northern Iran. *Geol. Soc. Amer. Bull.* **116** (*1–2*), 16–29.

Dempster T. J., Jolivet M., Tubrett M. N. and Braithwaiite C. J. R. (2003) Magmatic zoning in apatite: a monitor of porosity and permeability changes in granites. *Contributions to Mineralogy and Petrology* **145,** 568–577.

Ehlers T. A., Willett S. D., Armstrong P. A., and Chapman D. S. (2003) Exhumation of the central Wasatch Mountains, Utah; 2, Thermokinematic model of exhumaton, erosion and thermochronometer interpretation. *J. of Geophysical Research* **108 (B3),** 2173, doi: 10.1029/2001JB001723.

Farley K. A. (2002) (U-Th)/ He dating; techniques, calibrations, and applications. In *Noble gases in geochemistry and cosmochemistry*, Vol. Rev. in Mineralogy and Geochemistry. 47 (ed. D. Porcelli, C. J. Ballentine and R. Wieler), pp. 819–843. Mineralogical Society of America.

Farley K. A., Kohn B. P. and Pillans B. (2002) The effects of secular disequilibrium on(U-Th)/He systematics and dating of Quaternary volcanic zircon and apatite. *Earth and Planetary Science Letters* **201,** 117–125.

Farley K. A., Wolf R. A. and Silver L. T. (1996) The effects of long alpha-stopping distances on (U-Th)/He ages. *Geochim. Cosmochim. Acta* **60** (*21*), 4223–4229.

Gamble R. A., Wysoczanski R. J. and Meighan I. G. (1999) Contraints on the age of the Br. Tertiary volcanic province from ion microprobe U/Pb (SHRIMP) ages for acid igneous rocks from NE Ireland. *J. of the Geological Society of London* **156,** 291–299.

Hoskin P. W. O. and Ireland T. R. (2000) Rare earth element chemistry of zircon and its use as a provenance indicator. *Geology* **28,** 627–630.

House M. A., Wernicke B. P. and Farley K. A. (1998) Dating topography of the Sierra Nevada, California, using apatite (U-Th)/ He ages. *Nature* **396,** 66–69, doi:10.1038/23926.

House M. A., Wernicke B. P. and Farley K. A. (2001) Paleo-geomorphology of the Sierra Nevada, California, from (U-Th)/ He ages in apatite. *American J. of Science* **(301)**, 77–102.

Kirby E., Reiners P. W., Krol M., Hodges K., Farley K. A., Whipple K., Yiping L., Tang W. and Chen Z. (2002) Late Cenozoic uplift and landscape evolution along the eastern margin of the Tibetan plateau: Inferences from $^{40}Ar/^{39}Ar$ and U-Th-He thermochronology. *Tectonics*, doi: 10.1029/2000TC001246.

Mason P. R. D. and Mank A. J. G. (2001) Depth analysis by laser-ablation ICP-MS. In *Laser-Ablation-ICP-MS in the Earth Sciences: Principles and Applications*, Vol. Short Course 29 (ed. P. J. Sylvester), pp. 93–105. Mineralogical Association of Canada.

Meesters A. G. C. A. and Dunai T. J. (2002) Solving the production-diffusion equation for finite diffusion domains of various shapes; Part II, Application to cases with alpha -ejection and nonhomogeneous distribution of the source. *Chem. Geology* **186** (*1–2*), 57–73.

Min K., Reiners P. W., Nicolescu S. and Greenwood J. P. (2004) Age and temperature of shock metamorphism of Martian meteorite Los Angeles, from (U-Th)/He thermochronometry. *Geology* **32,** 677–680.

Min K., Reiners P. W., Wolff J. A., Mundil R. and Winters L. (2005) (U-Th)/He Dating of volcanic phenocrysts with high-U-Th inclusions, Lower Bandelier Tuff, Jemez Volcanic Field. *Chem. Geology*, In review.

Mitchell S. G. and Reiners P. W. (2003) Influence of wildfires on apatite and zircon (U-Th)/He ages. *Geology* **1025–1028**.

Nasdala L., Zhang M., Kempe U., Panczer G., Gaft M., Andrut M. and Plotze M. (2003) Spectroscopic methods applied to zircon. In *Rev. in Mineralogy and Geochemistry 53: Zircon* (ed. J. M. Hanchar and P. W. O. Hoskin), pp. 427–467.

Rahl J. M., Reiners P. W., Campbell I. H., Nicolescu S. and Allen C. M. (2003) Combined single-grain (U-Th)/He and U/Pb dating of detrital zircons from the Navajo Sandstone, Utah. *Geology* **31,** 761–764.

Reiners P. W., Brady R., Farley K. A., Fryxell J. E., Wernicke B. and Lux D (2000) Helium and argon thermochronometry of the Gold Butte Block, South Virgin Mountains, Nevada. *Earth and Planetary Science Letters* **178** (*3–4*), 315–326.

Reiners P. W. and Farley K. A. (1999) Helium diffusion and (U-Th)/He thermochronometry of titanite. *Geochim. Cosmochim. Acta* **63** (*22*),3845–3859.

Reiners P. W., Spell T. L., Nicolescu S. and Zanetti K. A. (2004) Zircon (U-Th)/He thermochronometry: He diffusion and comparisons with $^{40}Ar/^{39}Ar$ dating. *Geochim. Cosmochim. Acta* **68,** 1857–1887.

Reiners P. W., Zhou Z., Ehlers T. A., Xu C., Brandon M. T., Donelick R. A. and Nicolescu S. (2003) Post-orogenic evolution of the Dabie Shan, eastern China, from fission-track and (U-Th)/He thermochronology. *American J. of Science* **303,** 489–518.

Stockli D. F. and Farley K. A. (2004) Empirical constraints on the titanite (U–Th)/He partial retention zone from the KTB drill hole. *Chem. Geology* **207,** 223–236.

Stockli D. F., Farley K. A. and Dumitru T. A. (2000) Calibration of the apatite (U-Th)/He thermochronometer on an exhumed fault block, White Mountains, California. *Geology* **28** (*11*),983–986.

Stockli D. F., Surpless B. E., Dumitru T. A. and Farley K. A. (2002) Thermochronological constraints on the timing and magnitude of Miocene and Pliocene extension in the central Wassuk Range, western Nevada. *Tectonics* **21(4),** 1028, doi:10.1029/2001TC001295.

Tagami T., Farley K. A. and Stockli D. F. (2003) (U-Th)/ He geochronology of single zircon grains of known Tertiary eruption age. *Earth and Planetary Science Letters* **207** (*1–4*), 57–67.

Vavra G. (1993) A guide to quantitative morphology of accessory zircon. *Chem. Geology* **110,** 15–28.

Wolf R. A., Farley K. A. and Silver L. T. (1996) Helium diffusion and low-temperature thermochronometry of apatite. *Geochim. Cosmochim. Acta* **60** (*21*), 4231–4240.

Zeitler P. K., Herczeg A. L., McDougall I. and Honda M. (1987) U-Th-He dating of apatite; a potential thermochronometer. *Geochim. Cosmochim. Acta* **51** (*10*), 2865–2868.

Ziegler J. F. (1977) *Helium: Stopping Powers and Ranges in all Elemental Matter*. Pergamon.